ACS APPLIED POLYMER MATERIALS

pubs.acs.org/acsapm Article

# Biobased Multilayer Flexible Packaging with Enhanced Gas Barrier Properties due to Cellulose Nanocrystals (CNCs)

Jingxuan Zhang,[#] Yirou Wang,[#] Darien Anders Dewar, Akshat Verma, Nazmul Haque, Ronaldo Franjul, Nicole Stark, Chelsea S. Davis, and Jeffrey P. Youngblood*

Cite This: *ACS Appl. Polym. Mater.* 2025, 7, 6774−6788 Read Online

ACCESS | Metrics & More | Article Recommendations | Supporting Information

**ABSTRACT:** In this study, a transparent trilayer film was successfully fabricated using blade coating and hot roll lamination techniques, comprising outer layers of polylactic acid (PLA) and an inner layer of a highly shear-oriented cellulose nanocrystal (CNC)/poly(vinyl alcohol) (PVA). The CNC/PVA coating, with a thickness ranging from 5 to 6 $\mu$m and exhibiting a high degree of CNC alignment, significantly enhanced the oxygen and carbon dioxide barrier properties, surpassing PLA by several hundred-fold. Furthermore, these laminates were formed into bags, where a fruit storage test showed that PLA-CNC/PVA−PLA could extend the shelf life of fresh apple slices based on weight loss and enzymatic browning. This research showcases the potential of CNC-based coatings integrated with biodegradable polymer films to produce high-performance packaging materials, offering a promising, scalable process.

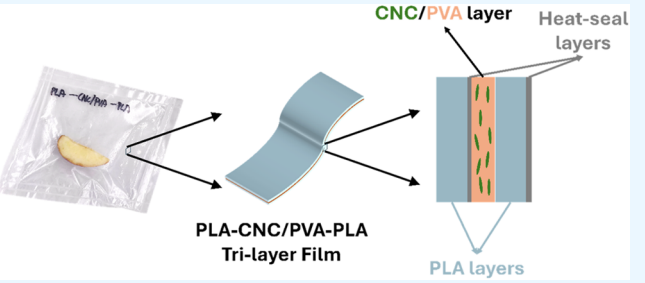


**KEYWORDS:** *cellulose nanocrystals, poly(vinyl alcohol), polylactic acid, food packaging, barrier, multilayer films*



## 1. INTRODUCTION

Petro-based polymeric films have been dominating the modern industry, such as food packaging,[1] electronics,[2] and construction,[3] for decades due to their low cost, flexibility, and low weight.[4] However, for most petrochemical plastics, it could take hundreds of years to decompose.[5] Unfortunately, food and beverage packaging is the main source of plastic litter along many coasts.[6,7] As plastic breaks into micro pieces, it can infiltrate the food web and result in serious health issues.[5,8−11] With all of these concerns, it is vital to develop sustainable and biodegradable packaging materials.

Cellulose is a ubiquitous natural polysaccharide, occurring in wood, plants, tunicates, algae, and bacteria.[12] It is biodegradable, carbon-neutral, and has low environmental or animal/human health risks.[12] Cellulose nanomaterials (CNMs) have been studied for decades. Among all of the cellulose nanomaterials, cellulose nanocrystal (CNCs) and cellulose nanofibrils (CNFs) are the two most commonly used or studied due to their abundance in plants.[12] CNCs are highly crystalline (54−88%), rodlike, or whisker-shaped materials produced by acid hydrolysis, with a high aspect ratio (3−5 nm wide, 50−500 nm long). CNFs are mechanically produced fine fibrils containing both crystalline and amorphous regions. The fibrils typically range in width from 4 to 20 nm and in length from 500 to 2000 nm.[4,12,13] Both CNCs and CNFs can be used as coatings to enhance the oxygen barrier performance. For most materials, a good oxygen barrier is generally not a good water barrier (and vice versa), as hydrophilic materials are good for oxygen barriers and hydrophobic materials are good for water barriers.[14,15] Regardless, CNC or CNF material oxygen barrier properties can outperform many synthetic polymers in relatively dry states, but their water barrier properties are much worse than most traditional barrier polymers like polypropylene (PP), polyethylene (PE), poly(ethylene terephthalate) (PET), or even polylactic acid (PLA).[14,16,17]

For cellulosic materials, the degree of crystallinity and aspect ratio heavily influences the barrier properties.[18] Additionally, the degree of anisotropy also plays an important role in the barrier properties by changing the packing density. For CNCs, upon acid hydrolysis, negatively charged sulfate groups are created on the surface of CNCs, and these groups repel each other electrostatically.[19] To minimize the interaction, CNCs in concentrated suspensions configure themselves into chiral nematic structures.[20,21] Due to their differences in dimensions, it is easier to form a highly aligned CNC coating than one from CNFs. Common alignment techniques include shear-based alignment,[22−26] magnetic field alignment,[27−30] and electric field alignment.[31−33] Currently, the shear-based alignment of

Received: January 30, 2025
Revised: May 22, 2025
Accepted: May 23, 2025
Published: May 29, 2025

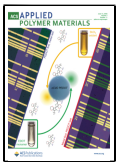

CNCs is the best method for mass production. Chowdhury et al.[34] utilized a Mirwec Mini-Labo Deluxe roll-to-roll Microgravure instrument to coat CNCs onto a PET substrate and achieved continuous processing with a uniform coating. Highly aligned CNCs have been proven to improve the oxygen and carbon dioxide barrier properties and enhance the mechanical properties. Similar to values reported by Chowdhury et al.,[14] Nuruddin et al.[35] discovered that the shear-oriented CNC film has a 16% lower fractional free volume compared to the chiral nematic CNC film, and the permeability of the shear-oriented CNC film was 95% lower than the chiral nematic structure for oxygen and 96% lower for carbon dioxide. Besides using aligned CNCs itself as the coating material on plastic substrates,[14,35] Nuruddin et al. incorporated CNCs with PVA and utilized the mixture as a coating on plastic substrates.[4,36] They found that the permeability values of oxygen and carbon dioxide were even lower[4] due to the free volume between CNCs being occupied by PVA; therefore, the overall diffusion paths were further suppressed.

Unfortunately, CNMs have poor water barrier properties and are sensitive to high humidity.[37] The simplest and most prevalent method to safeguard an oxygen barrier layer is by laminating another hydrophobic film onto it, which has been done as well for CNMs.[17] Koppolu et al.[38] used a roll-to-roll slot die to coat 2.5 wt % CNF and 3 wt % CNC suspension onto a paperboard substrate using cationic starch as the primer. The CNF-coated paperboard was later coated with LDPE or PLA by extrusion. Water vapor transmission rate (WVTR) results showed that CNM coatings showed a slight increase in the barrier properties. For OTR tests, the sample with the CNM layer showed more than a 90% decrease in the OTR values at 23 °C/50% RH, but their OTR values were the same as those of PLA samples at 38 °C/90% RH. This is because the paperboard has almost no barrier against moisture, and the hydrophilic CNM layers were still vulnerable toward moisture, resulting in a higher transmission rate. Le Gars et al.[39] mixed CNMs with rosin and prepared CNM−rosin self-standing films by solvent casting, and the films were later laminated between two PLA sheets by heat pressing. The oxygen permeability (OP) heat-pressed multilayered (TML) materials with CNCs reduced oxygen permeability to 1.23% compared to the reference group, which was prepared with an inner layer of PLA. However, the water vapor permeability increased in all multilayer films containing CNMs. This is attributed to the highly hydrophilic and brittle nature of the CNM layer, where microcracks could lead to an elevation in water permeability. Also, CNC freestanding films produced by solvent casting are generally much thicker than those produced by blade coating, and most solvent casting CNC films exhibit a low degree of alignment. Chen et al.[40] incorporated CNCs with PVA or kappa-carrageenan (CG) at various concentrations and coated them directly to a PLA substrate followed by lamination with another PLA layer. It was found that the three-layer laminated film showed a great decrease in oxygen permeability compared to PLA and water vapor permeability compared to pure CNC films, and outer PLA could protect the inner CNC layer from damage. However, the researchers tested only the oxygen barrier performance of the PLA-based films at 23 °C and 50% RH, and no oxygen barrier test was performed at higher humidity. Furthermore, no test was conducted in that paper on how well the trilayer films can be used as a real-life package for food.

In this paper, in an attempt to moderate the humidity sensitivity of CNCs as well as improve the oxygen barrier of PLA, a thin layer of the CNC/PVA coating was applied to the PLA substrate via blade coating, and the PLA film with the aligned CNC coating was later laminated with another PLA sheet, resulting in a biodegradable PLA-CNC/PVA−PLA trilayer system. The barrier performance against water, oxygen, and carbon dioxide was characterized at multiple humidities. The transparency of the multilayer films, the degree of alignment of the CNC/PVA inner layer, and the adhesion strength between CNC/PVA and the PLA substrate were also characterized. Unlike previous works, to understand potential applications, a fruit storage test was conducted to determine whether the PLA-CNC/PVA−PLA packaging can extend the shelf life of fruits. Specifically, cut apples were chosen due to their rapid browning and current use of additives on the surface of the fruit to prevent browning that affects their flavor and the need for transparent film materials.

## 2. EXPERIMENTAL SECTION

**2.1. Materials.** Poly(vinyl alcohol) (PVA) ($M_w$ of 89,000−98,000 with 99% hydrolysis) was purchased from Sigma-Aldrich. The never-dried 11.7 wt % cellulose nanocrystal (CNC) aqueous suspension (0.99 wt % sulfur on dry CNC, Batch# 2016-FPL-CNC-098-UF) was purchased from the University of Maine (Orono, ME). The polylactic acid (PLA) film of approximately 30 $\mu$m with a one-side heat-seal layer (trade name: Evlon Compostable Film, model number 30EVHS1) was purchased from Bi-Ax International Inc. (Wingham, ON, Canada). The heat-seal layer was a layer of PLA with a relatively lower molecular weight compared with that of PLA from the substrate. Linear polarizers with 42 ± 2% single-pass transmission (model: AP42-004T) were purchased from American Polarizers, Inc. (Reading, PA). Dry oxygen and carbon dioxide gas tanks were purchased from Indiana Oxygen (Lafayette, IN) with purities of 99.5 and 99.9%, respectively.

**2.2. Preparation of the PVA Solution and CNC/PVA Mixture.** PVA powders (11.7 g) were mixed with 88.3 g of DI water in a round-bottom flask and heated to 80 °C with constant stirring until a clear solution was obtained. Then, the 11.7 wt % PVA solution was mixed with the 11.7 wt % CNC suspension at a 30:70 weight ratio inside a 200 mL mixing cup to achieve a 11.7 wt % 70 CNC-30 PVA mixture. Previous work indicated that the 70:30 ratio showed a relatively low $O_2$ and $CO_2$ permeability and the highest contact angle when coated on a PP substrate.[4] Also, the 70 CNC-30 PVA mixture showed the highest anisotropy.[41] Unless mentioned otherwise, the CNC/PVA mixture in the following paragraphs means the 11.7 wt % 70 CNC-30 PVA mixture. The mixture was later mixed at 2500 rpm for 5 min using a SpeedMixer system (Flacktek Inc.) to mix and fully remove bubbles from the mixture.

**2.3. Application of the CNC/PVA Coating onto the PLA Substrate.** CNC-PVA was applied to the PLA film in a manner similar to that previously reported.[4,24,35,36] Briefly, the PLA film was cut into a square of approximately 9″ × 9″. It was then secured to a glass sheet of approximately 10 in. x 10 in. x 1/8 in. using masking tape with a thickness of around 130 $\mu$m and in such a way to control the thickness of the coating. The heat-seal layer of the PLA film was against the glass sheet so that the CNC-PVA coating would be applied to the side without the heat-seal layer. A BD-20AC laboratory corona treater (Electro-Technic Products, Chicago) was used to treat the polylactic acid (PLA) film surface for about 5 min by "scanning" the film to improve the surface energy of the PLA film for better compatibility with the hydrophilic CNC/PVA coating. The corona-treated PLA substrate was coated with the CNC/PVA coating via the "blade-coating" method using a long ruler with a 45° alignment to the suspension. Immediately after the coating process, the films were dried in an oven at 60 °C for 10 min, stored in a relatively low-humidity condition, and taken off from the glass sheet after the


https://doi.org/10.1021/acsapm.4c03954
ACS Appl. Polym. Mater. 2025, 7, 6774−6788

sample was fully dried to minimize the curling of the CNC/PVA-coated PLA sheets.

**2.4. Lamination of PLA-CNC/PVA−PLA Trilayer Films.** The layered structure of PLA-CNC/PVA−PLA was produced by a hot roll laminator. The laminator was set at single-sided heating mode with only the top roll being heated, and the temperature was set at 80 °C. Another PLA film with a heat-seal layer was placed on the top of the CNC/PVA coating with the heal-seal layer facing the coating, and then, two films were fed into the laminator. The layered films were laminated in one direction twice, rotated 90°, and laminated twice to remove possible air bubbles or wrinkles. Eventually, a trilayer PLA-CNC/PVA−PLA film was made. The lamination process takes about 6 s for each run. A schematic plot of the coating and lamination process is shown in Figure 1.

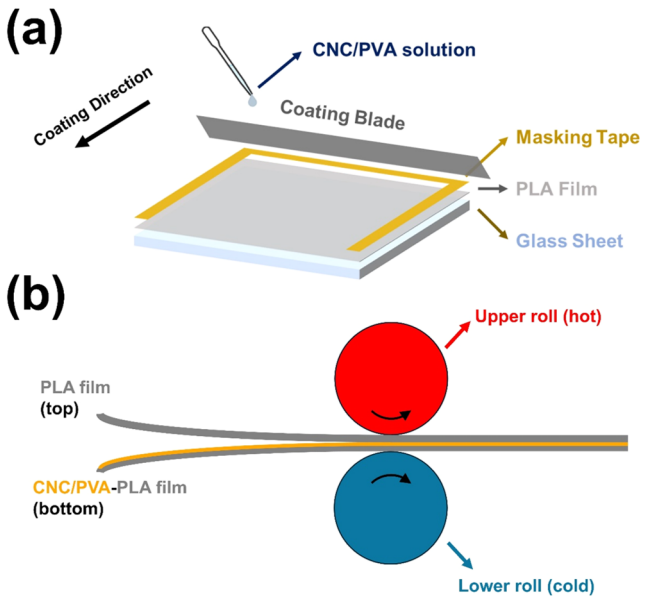


**Figure 1.** Schematic plot of (a) the CNC/PVA−PLA coating process and (b) the PLA-CNC/PVA−PLA lamination process.

**2.5. Morphology and Surface Chemistry Characterization.** A FEI Teneo VolumeScope system (Thermo Fisher Scientific, Waltham, MA) was used to generate scanning electron microscopy (SEM) images of the cross-sections of the multilayered films. The working distance was about 10 mm, with a voltage of 5 kV. The samples were cut using a sharp blade, and ∼2 nm of Pt was sputtered using a Cressington 208HR sputter coater (Cressington Scientific Instruments, Watford WD19 4BX, U.K.) over 60 s during sample preparation. In addition, thickness measurements were also conducted at various points of different samples using a digital micrometer (Mitutoyo, Japan), with at least five sets of measurements taken for each sample. An AmScope polarized-light microscope with a MU Series 18.0MP USB 3.0 Color CMOS C-Mount microscope camera was also used to generate the microscopic surface of the CNC/PVA coatings.

A Bruker Dimension Icon atomic force microscope (Bruker Corporation, MA) in tapping mode was employed for the assessment of the surface roughness of the pristine PLA and CNC/PVA-coated PLA samples. A soft tapping mode AFM probe tip ($\mu$-mash, HQ-NSC18/AIBS) was used for the characterization. The samples were first cut from the middle part of the films and then taped onto magnetic disks for mounting. Sections of 40 $\mu$m × 40 $\mu$m were imaged.

A PerkinElmer Spectrum 100 FTIR spectrometer (ATR-FTIR) was used to characterize the surface coating, aiming to confirm the successful coating of CNC-PVA onto the PLA surface and characterize the composition of commercial packaging bags. A background scan was first collected, and then the samples were placed in direct contact with the crystal during testing. Twenty scans were collected for each run over 600−4000 $cm^{-1}$ with a 1 $cm^{-1}$ resolution.

**2.6. Optical and Anisotropic Measurement of the CNC Coating.** The transparency of the films and the degree of alignment for the CNC coating were investigated using a UV−vis spectrophotometer (Agilent Cary 6000i UV−vis−NIR spectrophotometer, Agilent Technologies, Inc.) using the ATSM D1746-23 standard.[42] For the transparency measurement, air was taken as the 100% transparency standard, and then the transmission mode was used to test different films in the visible-light range.

The detailed methods for the degree of alignment measurement were previously reported in the literature.[4,14,24,35] Due to the biaxial stretching process employed in the production of the PLA films, inherent birefringence is observed, posing challenges in the assessment of CNC layer alignment. Also, freestanding CNC films are very brittle, and it is almost impossible to prepare anisotropic films with large dimensions.[14] Henceforth, CNC/PVA was applied onto glass substrates employing an identical coating methodology as employed for the PLA film, given the nonbirefringent nature of glass substrates and their elevated surface tension relative to CNC/PVA. Subsequently, CNC/PVA-coated glass specimens were interposed between two orthogonal linear polarizers, and the intensity of transmittance spanning the wavelength range of 400 to 750 nm was assessed in the 45 and 90° configurations, respectively. The Herman's order parameter of the coating was calculated from the following equations:

$$I_\theta = I_0 \sin^2 2\theta \sin^2\left(\frac{\pi \Delta n d}{\lambda}\right) \tag{1}$$

$$\frac{I_{45}}{I_{90}} = \frac{I_0 \sin^2(2 \times 45^\circ)\sin^2\left(\frac{\pi \Delta n d}{\lambda}\right)}{I_0 \sin^2(2 \times 90^\circ)\sin^2\left(\frac{\pi \Delta n d}{\lambda}\right)} \tag{2}$$

$$\frac{I_{45}}{I_{90}} = D^* = D \cdot g = \frac{(2S + 1)}{(1 - S)} \tag{3}$$

where $I_\theta$, $I_0$, $\theta$, $\Delta n$, $d$, $\lambda$, $D^*$, $D$, $g$, and $S$ represent the transmitted light intensity for the $\theta$ configuration, amplitude of the incident light, angle of the coating direction regarding the cross-polarizers, refractive index differences, thickness of the coated film, wavelength, true dichroic ratio, dichroic ratio, correction factor, and the Herman's order parameter. Here, we consider $g = 1$ for order parameter calculation.[24] For perfectly aligned arrangements, $S = 1$; for the completely random or chiral nematic configuration, $S = 0$.

**2.7. Water Vapor Transmission Rate (WVTR) Measurement.** The water vapor transmission rate (WVTR) is defined as the mass of water vapor penetrating through the membrane per unit area and per unit time, and it is used as a parameter for measuring water barrier properties. WVTR assessments were conducted utilizing small permeation cups sourced from Gardco Inc., in adherence to the guidelines outlined in ASTM D1653-13.[43] Both dry and wet condition testing was performed. For dry testing, about 4 g of the desiccant was placed into the cup, while the wet testing had around 5 g of water in the cup instead of the desiccant. The samples were cut into a circular shape that was slightly larger than the opening of the perm cup so that the sample fully covered the cup and the samples were sealed between two O-rings and screwed tightly. The cups were weighed every 24 h. Both dry and wet testing was performed at room temperature of 23 °C and 50% relative humidity. Initial testing showed that the 100% humidity condition compromised the CNC/PVA layer, and so all testing was performed with PLA to the high humidity side. To maintain data consistency, trilayer specimens were performed in an identical arrangement to the bilayers.

In an effort to both confirm perm cup testing and show the WVTR behavior in the "swamp" conditions of high humidity and temperature, the WVTR was also determined according to ASTM F1249 using a Permatran-W 3/34 G WVTR analyzer (Ametek Mocon, Minneapolis, MN). The cell temperature was 37.8 °C. A carrier gas


https://doi.org/10.1021/acsapm.4c03954
ACS Appl. Polym. Mater. 2025, 7, 6774−6788

(nitrogen) entered the top half of the cell, while the test gas entered the bottom half of the cell. Three replicates were run for each series of tests.

The film water vapor permeability (WVP) for both sets of data was calculated using the following equation:

$$\mathrm{WVP} = \frac{\mathrm{WVTR}}{(R_1 - R_2) \times \mathrm{SVP}} \tag{4}$$

where SVP is the saturation vapor pressure of water at the test temperature ($S_{38°C}$ = 6538 Pa), $R_1$ is the fractional RH on the vapor source side (50%), $R_2$ is the fractional RH on the sink side (0%), and $l$ is the film thickness.

**2.8. Gas Permeability Measurement.** The oxygen and carbon dioxide permeability values were measured in two different ways. For gas permeability at room temperature, 0% RH, the test was according to the previous research.[4,14,36] Briefly, the sample was cut into a circle with a diameter of 25 mm and then inserted into a stainless-steel holder with an exposed area of 3 $cm^2$. The whole system was first vacuumed for around 15 min to remove residual air and moisture, and then the valve connected to the holder was closed to prevent air from entering the holder from outside. The leak rate is defined as the slow pressure rise in the downstream volume due to leakage of the system. After 10 h, the valve connecting the top of the sample holder was opened to let the test gas fill the upper part of the holder. Therefore, a pressure difference was created between the two sides of the sample, where one side was almost vacuum and the other side had a pressure of around 50 psi of the test gas. The testing generally lasts for 3−5 days, depending on the barrier property of the sample against test gas. Equation 5 was used to calculate the permeability of the film.[44]

$$P = \frac{V_d l}{P_2 A R T}\left[\left(\frac{dp}{dt}\right)_{ss} - \left(\frac{dp}{dt}\right)_{leak}\right] \tag{5}$$

where $P$ is the permeability of the film, $V_d$ is the downstream volume, $l$ is the thickness of the film sample, $P_2$ is the upstream absolute pressure, $A$ is the exposed area of the film, $R$ is the gas constant, and $T$ is the absolute temperature. $(dp/dt)_{ss}$ and $(dp/dt)_{leak}$ are the steady-state pressure rise vs time during the permeability and leak tests, respectively.

For the sample with two layers, the overall permeability was calculated using eq 6:[45]

$$P_c = \frac{h_c}{\frac{h_1}{P_1} + \frac{h_2}{P_2}} \tag{6}$$

where $P_c$ is the overall permeability, and $h_c$ is the total thickness of the film. $h_1$, $h_2$, $P_1$, and $P_2$ are the thickness and the permeability of each layer, respectively. If there is no interaction between the layers of the multilayer material, under ideal conditions, eq 6 can be extended to the following equation:

$$P_c = \frac{h_c}{\sum_{i=1}^{n} \frac{h_i}{P_i}} \tag{7}$$

where n is the number of layers, and $h_i$ and $P_i$ are the thickness and permeability of individual layers, respectively.

A high−low humidity cycle test for CNC/PVA−PLA and PLA-CNC/PVA−PLA samples was conducted by first placing samples in an environment of 28.5 °C, 95% RH for 24 h. Later, the films were put back to room temperature and 50% RH for another 24 h. Then, the $O_2$ permeability values of these two samples were tested at room temperature and 0% RH using the pressure loss method mentioned above.

To further explore how well PLA layers can protect the inner CNC/PVA layer, a dry-water-dry cycle test for the PLA-CNC/PVA−PLA film was conducted. PLA-CNC/PVA−PLA films were submerged in DI water at room temperature for 2 h. Later, the films were wiped and the sample was dried at room temperature, 50% RH for 30 min, and then its $O_2$ permeability was tested at room temperature, 0% RH.

The samples were also tested at different relative humidity values according to ASTM D3985 using an Ox-Tran 22/2 L OTR analyzer (Ametek Mocon, Minneapolis, MN). The cell temperature was 23.0 °C and both the test gas and carrier gas were at the same relative humidity. The carrier gas entered the top of the sample holder, while the test gas entered the bottom. Three replicates were run for each series of tests. The oxygen permeability (OP) was calculated in the same way as in eq 4 except for using the oxygen transmission rate in the numerator.

**2.9. Mechanical Tests for the Multilayer Films.** The uniaxial tensile test was performed under the ASTM D638 standard, and the T-peel test was done according to the ASTM D1876 standard. A TA.XTplusC texture analyzer (Stable Micro Systems, Godalming, United Kingdom) was used for both tests.

For the uniaxial tensile test, the samples were first cut into a standard shape. PLA, CNC/PVA−PLA, PLA−PLA, and PLA-CNC/PVA−PLA were tested. The test speed was set at 10 mm/min. The samples were pulled until break. Force and displacement values were recorded at a frequency of 200 points per second.

For the T-peel test, the PLA−PLA samples were used as the control group, while the PLA-CNC/PVA−PLA samples were the experimental group. To prepare peeling test samples, for every plastic sheet, the sheets were only laminated halfway up the length, leaving the other half unbonded. Then the plastic sheet was cut into long, narrow rectangular strips perpendicular to the lamination boundary line. The width of each strip was approximately 20 mm. Then, the two unbonded ends were clamped in two test grips and tightly screwed. A constant head speed of 10 in./min was applied until all of the laminated parts were peeled off. The test was done at room temperature (20 °C) and 50% RH.

Adhesion between the CNC/PVA coating and the PLA substrate was also tested by a "cross-hatched peel" test according to the ASTM D3359-23 standard using two replicates. A multiblade cutter with 11 teeth and 2 mm spacing was used to cut the lattice on top of the CNC/PVA−PLA film. A pressure-sensitive tape was applied to the sample and the sample was pressed firmly. Later, the tape was peeled off, and the coating was inspected and rated accordingly.

**2.10. Fruit Storage Test of Multilayer Films.** Two specimens each of PLA−PLA and PLA-CNC/PVA−PLA multilayer films were procured and subsequently trimmed to square dimensions of 7″ × 7″. The specimens of each multilayer film type were then superimposed, and three edges were sealed utilizing an impulse heat sealer (Model: PFS-300, Jinhong Plastics, China) with double sealing at each side at level 4 of the impulse power. This process resulted in the fabrication of pouches composed of either PLA−PLA or PLA-CNC/PVA−PLA multilayer films. A sterilized apple cutter was used to cut red delicious apples purchased from a local grocery store into eight wedges. One wedge was weighed quickly and then placed in the pouch. A small oxygen concentration sensor (Honeywell BW Solo wireless gas detector O2 BWS1-XL-Y, Honeywell, Charlotte, NC) was also placed inside another pouch of the same material to measure the oxygen concentration inside. The pouch was then purged with nitrogen gas using an air nozzle, and then the remaining open edge of the pouch was sealed with the impulse heat sealer. Periodically, the bags were weighed. Furthermore, PLA−PLA pouches each having an apple wedge inside were left unsealed and used as the control group, and commercial bags that had already been used as apple slice packaging bags were utilized as a comparison. We utilized a CIELAB color space colorimeter (model: WR-10QC, FRU Inc., China) to measure six different spots (the top end, middle part, and bottom end of each side) of the apple wedges through the PLA-based pouch material every 24 h, as shown in Figure S1. Furthermore, the oxygen concentration within the pouch and changes in the total weight were recorded daily. The samples were stored under two conditions: (a) room temperature (23 °C) and around 50% relative humidity and (b) in a fridge (4 °C) and around 10% relative humidity.



https://doi.org/10.1021/acsapm.4c03954
ACS Appl. Polym. Mater. 2025, 7, 6774−6788

**2.11. Statistical Analysis.** Data were analyzed using the *t*-test and one-way analysis of variance (ANOVA) via Tukey's HSD based on 95% confidence intervals.

## 3. RESULTS AND DISCUSSION

**3.1. Morphology and Surface Properties.** A series of tests were conducted to determine the thickness of the specimens using a micrometer. For each sample, we measured different locations of different specimens. The test results are listed in Table 1. The coating weight was calculated by comparing the weight of the coated sample before and after. Five specimens from different samples were collected, and results showed that the coating weight was 8.4 ± 0.5 grammage.

**Table 1. Thickness of PLA, CNC/PVA−PLA, PLA−PLA, and PLA-CNC/PVA−PLA Films**[a]

| film | thickness [$\mu$m] ± STD |
|---|---|
| PLA | 28.4 ± 1.0 |
| CNC/PVA−PLA | 34.0 ± 1.7 |
| PLA−PLA | 57.1 ± 1.0 |
| PLA-CNC/PVA−PLA | 65.5 ± 1.0 |

[a]The error is one standard deviation.

As can be seen from Table 1 and Figure 2, the thickness of the CNC/PVA coating is about 1/6 to 1/5 of the PLA substrate. In addition, the cross-sectional SEM images revealed that the CNC/PVA coating appeared "fragmented" after being cut, which is attributed to the inherently brittle nature of CNCs.

Figure 3 shows the images of CNC/PVA−PLA films prepared by shear coating and solvent casting. It could be observed that the shear-coated CNC/PVA formed a continuous and aligned structure on PLA, although the PLA film was prepared by biaxial stretching and has a certain birefringence. The solvent-cast CNC/PVA layer showed the characteristic chiral nematic structure. It was also found from the polarized-light microscopy images that an aligned pattern was observed on the shear-coated CNC/PVA samples. Also, the light intensity shown in Figure 3d was much higher than that shown in Figure 3e. This was because the shear-aligned CNC/PVA-coated sample was placed 45° against the cross-polarizers, while the chiral nematic nature of the CNC/PVA-coated sample did not focus the light intensity to any certain angle.

To further prove that PLA has been successfully coated, ATR-FTIR tests were conducted. Figure S2 shows the ATR-FTIR test results of the PLA substrate, the CNC/PVA coating itself, and the CNC/PVA−PLA film samples. The CNC/PVA curve showed a wide peak at 3334 $cm^{-1}$ (O−H stretching) and a sharp peak at 2911 $cm^{-1}$ (C−H stretching). Peaks at 1653, 1430, 1319, and 1035 $cm^{-1}$ are the typical peaks for cellulose. For the PLA sample, peaks at 3000 $cm^{-1}$ (C−H stretching), 2955 $cm^{-1}$ (C−H stretching), and 1748 $cm^{-1}$ (O═H stretching) were characteristic function groups. For the CNC/PVA−PLA sample, the FTIR curve was almost identical to the CNC/PVA coating itself, and this confirmed the existence of the CNC/PVA coating on PLA film.

**3.2. Mechanical Test of the Multilayer Films.** The uniaxial tensile test was conducted to characterize and compare the mechanical properties of the different films. Figure 4 compares the results of the tensile test, including the Young's modulus, yield stress, fracture stress, and strain at break, for the four types of PLA-based films. Detailed stress versus strain curves are plotted in Figure S3, and the photos of four samples after the test are shown in Figure S4. For the Young's modulus, based on ANOVA using Tukey's test, the Young's modulus of PLA films was higher than other three groups. However, it is worth noting that the difference of the Young's modulus among groups was not very high. Another reason could be that all films experience some thermal history, either hot roll lamination or oven drying, except the PLA film. This history might be the reason for the difference in the Young's modulus, as the crystallinity and crystal size might be different before

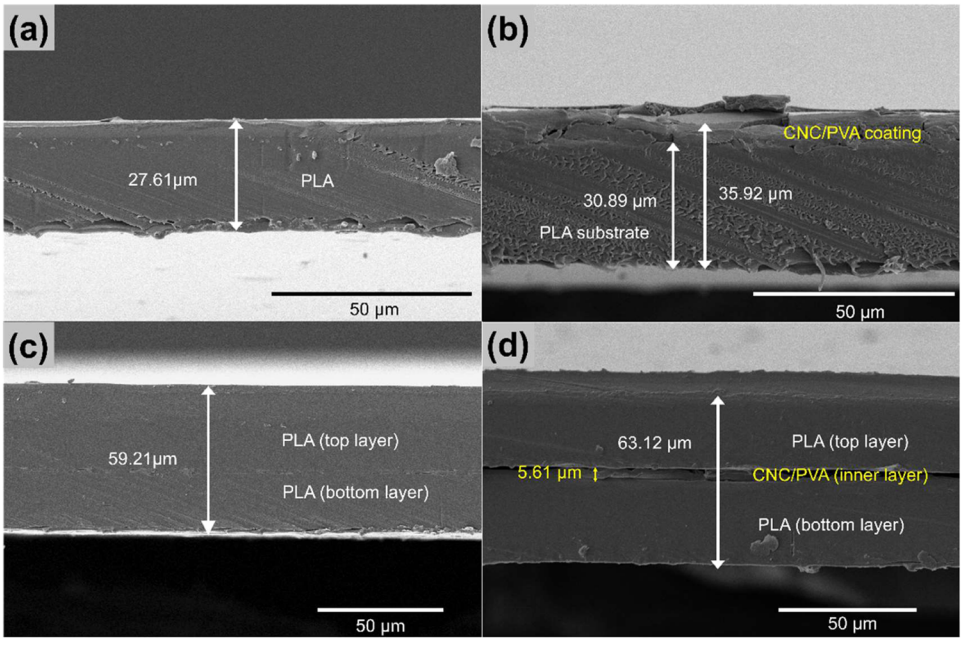


**Figure 2.** SEM images of the cross-section of (a) PLA, (b) CNC/PVA−PLA, (c) PLA−PLA, and (d) PLA-CNC/PVA−PLA film samples.



https://doi.org/10.1021/acsapm.4c03954
ACS Appl. Polym. Mater. 2025, 7, 6774−6788

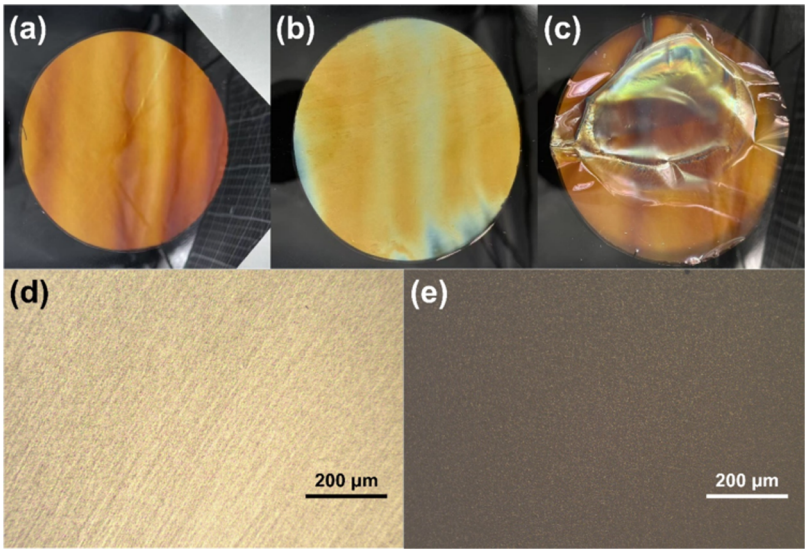


**Figure 3.** Photos of (a) plain PLA, (b) shear-coated CNC/PVA−PLA, and (c) solvent-cast CNC/PVA−PLA. Polarized-light microscopy images of CNC/PVA on plain glass via (d) shear coating and (e) solvent casting.

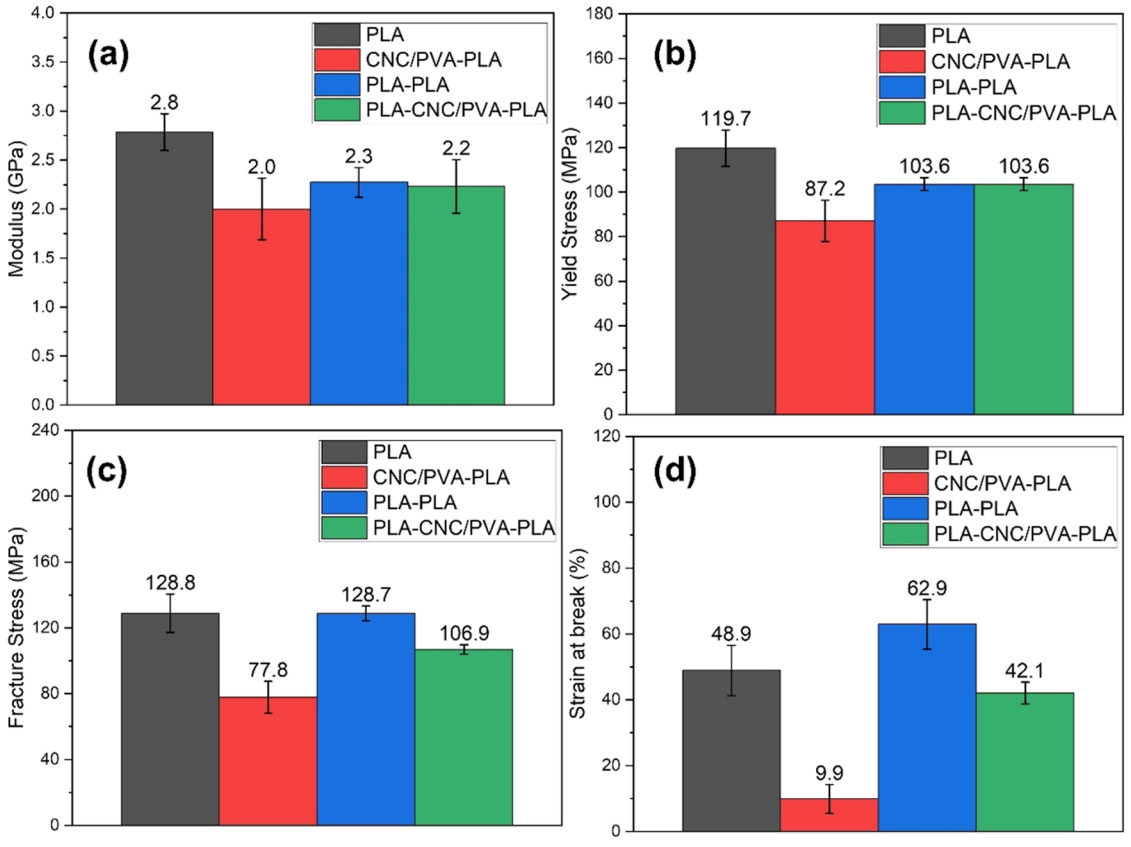


**Figure 4.** Tensile test results for the four types of films: (a) modulus, (b) yield stress, (c) fracture stress, and (d) strain at break.

and after the heat treatment. For the yield stress, fracture stress, and strain at break, the CNC/PVA−PLA film showed lower values compared with other three films. This phenomenon could be that the CNC/PVA layer is a more brittle layer compared with the PLA substrate, therefore resulting in a more brittle behavior in the tensile test. For PLA-CNC/PVA−PLA, the mass ratio of brittle to ductile layers was only half of the CNC/PVA−PLA sample. Also, from Figure S4d, it could be found that before the fracture happened, the stress first dropped, then increased a little bit, and then dropped again. This could be due to the relatively low adhesion force between the layers. During the final stage, one layer first broke, causing the first stress reduction; then, the other layer became the load-bearing unit and resulted in a small stage of stress rise. Later, the second layer broke eventually, causing the stress to reduce for the second time. A similar behavior has been reported in a previous study on CNF-coated samples by our group.[16] For PLA−PLA, no such



https://doi.org/10.1021/acsapm.4c03954
ACS Appl. Polym. Mater. 2025, 7, 6774−6788

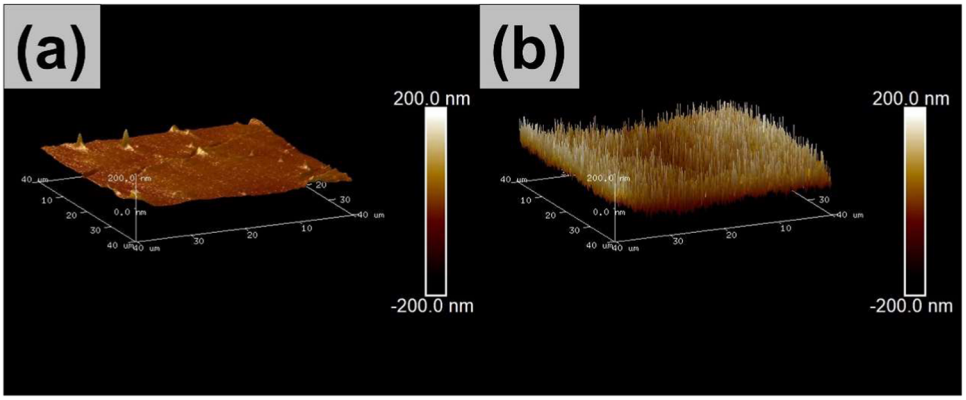


**Figure 5.** AFM images of (a) pristine PLA and (b) the CNC/PVA-coated PLA sample surface.

pattern was observed in the stress vs strain curve, indicating a relatively higher adhesion force between the PLA layers, as the two layers of PLA broke at the same time. The photos shown in Figure S4 also indicated the same behavior.

The T-peel test was conducted to characterize the adhesion strength between the material layers. Adhesion strength, or normalized force, is measured as the force over the sample width when the sample is pulled at a specific speed. Figure S5 is a schematic plot showing how the test was conducted, and the detailed values of the normalized force vs peeling distance are plotted in Figure S6. After peeling initiation, the normalized force values fluctuate around a consistent value, aligning with previous findings.[46] Also, as shown in Figure S7, during the peeling process, the "tail" of the sample (i.e., the portion that has not yet been peeled) exhibits certain amplitude oscillations. The average normalized force per width values for PLA−PLA and PLA-CNC/PVA−PLA are 100.0 ± 13.7 and 24.1 ± 6.5 N/m, respectively. Samples without the CNC/PVA intermediate layer exhibit higher adhesion strength, which also agrees with our rationale for the "stair-like" pattern in the stress vs strain curve of the PLA-CNC/PVA−PLA film. The reduction of adhesion force could be attributed to the increased surface roughness facilitated by CNC/PVA, which has been further confirmed by the AFM images shown in Figure 5. As depicted in the picture, the CNC/PVA-coated PLA sample exhibited a much higher roughness than the pristine PLA sample, consistent with previous studies.[41,47] Fortunati et al.[48] also observed that the addition of CNCs led to an increase in the surface roughness of the PVA/CNC film, which could be due to the much higher degree of crystallinity of CNCs, the relatively high concentration of the CNC/PVA solution, and the spindle-shaped morphology of CNCs. This also explains the slight difference in the calculated thickness of the inner CNC/PVA layer by comparing the thickness of CNC/PVA−PLA and PLA vs comparing between PLA-CNC/PVA−PLA and PLA−PLA. During lamination, the rougher coatings created larger gaps between layers compared to smoother surfaces. Increasing the lamination temperature further would likely soften the outer layer of the PLA film. The PLA film itself would adhere to the heated roller, causing lamination failure. Furthermore, the heat-seal layer made of PLA with a relatively low molecular weight cannot fully melt into a liquid state. This prevents mechanical interlocking between the heat-seal layer and the CNC/PVA layer, reducing the contact area and resulting in a decreased adhesion strength. Lawniczak et al. studied the relationship between peel strength and surface roughness and found that the average 90° peel force decreases as the degree of substrate roughness increases. Ozer explored[49] the effect of substrate roughness on the peel force for tape peeling. It was found that the peel force was smaller when peeling a tape from a rough substrate than a smooth substrate, and an increased root-mean-square (RMS) roughness decreases the peel force for tape peeling.

To further determine whether the fracture in the peel test was due to adhesive failure between the coating and the substrate or due to cohesive failure of ripping off from the substrate, food coloring dye was added to the CNC/PVA solution. The colored CNC/PVA solution was coated onto the PLA substrate followed by the lamination and peel test. Figure S8 shows the before and after T-peel test photos. From the photos, it is clear that the PLA top layer has very few observable pink dots from CNC/PVA. This indicates that the failure type was mostly adhesive rather than cohesive. The adhesive strength between the CNC/PVA coating and the PLA bottom layer was higher than that between the PLA top layer and the CNC/PVA coating. However, it must be noted that the relationship between the geometry of the substrate and the peel strength is very complicated. To our knowledge, the value of the peel strength could be influenced by the roughness, peeling angle, speed of peeling, etc. In other words, if those parameters are different, the peel strength could be very different. Nevertheless, the main purpose of this paper is to study the barrier performance of the multilayer films, and the peel strength is not the most critical part of this paper and needs another new research to be fully understood.

As observed from the SEM images, CNC/PVA was very brittle. Therefore, it is impossible to measure the adhesive strength between the CNC/PVA coating and the PLA substrate by performing a peel test. In order to characterize the adhesion between the CNC/PVA coating and the PLA bottom substrate, a "cross-hatch" peel test was performed. Figure S9 shows a photo of the coating before and after the test. We have observed that there is no significant difference on the surface of the sample before and after testing. According to the ASTM D3359-23 standard, it was classified as grade 5B, indicating that no areas are detached and that the adhesive strength between the coating and the substrate is strong. However, it is important to note that the tape test itself is a relatively coarse qualitative testing method and more suitable for a soft coating on a hard substrate. We can only make a rough assessment of adhesive strength.

**3.3. Transparency of the Films and Order Parameter of the Coating.** For food packaging materials, transparency



https://doi.org/10.1021/acsapm.4c03954
ACS Appl. Polym. Mater. 2025, 7, 6774−6788

has been particularly important, as consumers can visually assess the appearance and condition of the food. For polymeric materials, numerous factors can influence transparency, such as crystallinity, processing techniques, additives, thickness, etc. A common method for measuring material transparency is by assessing its transmittance, which involves using a UV−visible spectrophotometer to test the material within the visible-light spectrum.[50] This testing method is relatively straightforward and allows for quantitative description and comparison of the transparency of different materials by using percentages.

Figure 6 shows the transmittance value for the PLA film, the CNC/PVA-coated PLA film, the PLA−PLA film, and the trilayer PLA-CNC/PVA−PLA film. The transmittance values within the visible-light spectrum (380−700 nm) were collected and averaged for the purpose of comparison. The PLA film exhibited the highest transmittance (93.8%), followed by CNC/PVA−PLA (91.6%), PLA−PLA (84.6%), and PLA-CNC/PVA−PLA (83.4%). It was evident that the transparency decreased for the CNC/PVA−PLA samples compared to pristine PLA, which could be possibly due to the inherently higher degree of crystallinity of the CNC/PVA coating scattering mire light. For the triple-layer PLA-CNC/PVA−PLA configuration, the thickness approximately doubles as compared with the previous configuration, leading to a further reduction in transparency. Nevertheless, all four films exhibited a transmittance value higher than 80%, and thus, they can be classified as transparent polymer materials. All four films also provided UV protection at UV-C (100−280 nm) but did not significantly contribute to UV-A (315−400 nm) and UV-B (280−315 nm). A photo of the four different films is also shown in Figure S10.

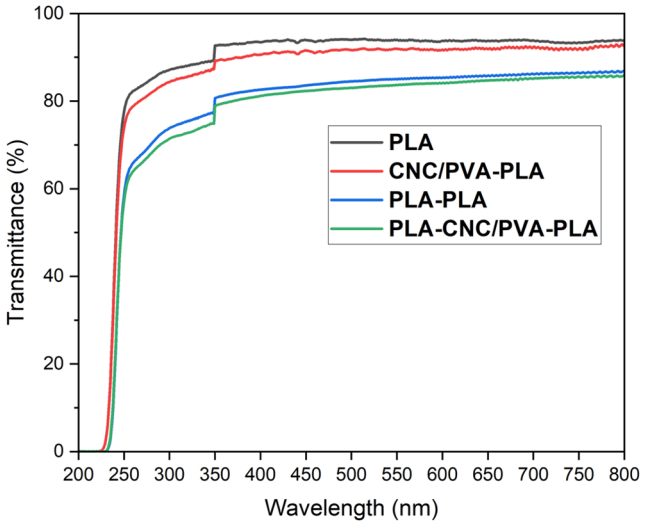


**Figure 6.** Transmittance vs wavelength for PLA, CNC/PVA−PLA, and PLA-CNC/PVA−PLA films. Note: the step change at ∼350 nm is due to the source switchover.

To characterize the alignment of the CNC/PVA films, two CNC/PVA-coated glass samples were placed between cross-polarizers at 90 and 45° angles, as shown in Figure S11. As previously mentioned, PLA samples exhibit a pronounced birefringence, which would substantially diminish the signal-to-noise ratio if CNC/PVA-coated PLA samples were directly assessed. Therefore, we opted to apply the coating onto glass substrates for subsequent testing since glass exhibits no birefringence. The method of coating CNC/PVA onto the glass substrate was the same as that on PLA except that corona treatment was not needed due to the high surface energy and hydrophilicity of the glass. It was observed that the transmittance value of the sample at 45° was significantly higher than that at 90°. Based on the four samples, the average order parameter ($S$) was 0.84, indicating that the CNC/PVA coating exhibited a high degree of anisotropy, which has been shown to be beneficial for a high barrier performance.

**3.4. Barrier Properties of the Films.** To characterize the water vapor barrier properties of the films, the water vapor transmission rate (WVTR) was measured by both the "dry-cup" and "wet-cup" methods. The dry cup measures the water transport across a film from a moderate (50%) humidity to a low (0%) humidity and is representative of low humidity conditions, while the wet cup measures water transport across a film from a water filled cup nominally at ∼100% humidity to a chamber of 50% humidity and is representative of high humidity conditions. For certain materials, especially hydrophilic ones, the WVTR values measured using dry-cup and wet-cup methods may exhibit significant differences due to plasticization of the material due to humidity.

Table 2 shows the WVTR and WVP values for PLA, CNC/PVA−PLA, PLA−PLA, and PLA-CNC/PVA−PLA samples under the dry-cup and wet-cup conditions. In the dry-cup testing method, a decrease of about 20 g/(m$^2$·day) in the WVTR for PLA samples with the CNC/PVA coating is observed compared to those without the coating. The CNC/PVA coating increases the overall thickness, and the WVTR is inversely proportional to the thickness. However, the thickness of the CNC/PVA coating itself is quite small (∼6 μm) compared to the PLA substrate (∼30 μm). Thus, the WVTR was normalized by thickness into water vapor permeability (WVP), where the WVP value also decreased under dry-cup tests. This is likely due to the low free volume in the aligned films and the high crystallinity of the CNC, even if the materials are quite hydrophilic. However, in the case of the wet-cup method, it is observed that the presence or absence of the CNC/PVA coating does not have a significant impact on the WVTR values, and the presence of the CNC layer

**Table 2. Water Vapor Transmission Rate (WVTR) and Water Vapor Permeability (WVP) for PLA, CNC/PVA−PLA, PLA−PLA, and PLA-CNC/PVA−PLA Film Samples under Dry-Cup and Wet-Cup Methods**[a]

| | WVTR [g/(m$^2$·day)] | | WVP [g·μm/m$^2$·day·kPa] | |
|---|---|---|---|---|
| sample | dry cup | wet cup | dry cup | wet cup |
| PLA | 45.1 ± 3.1 | 55.9 ± 1.5 | 808.1 ± 55.5 | 1001.7 ± 26.9 |
| CNC/PVA−PLA | 25.4 ± 2.6 | 54.5 ± 1.6 | 544.9 ± 55.7 | 1169.1 ± 34.3 |
| PLA−PLA | 26.6 ± 1.5 | 29.9 ± 1.6 | 958.3 ± 54.0 | 1077.2 ± 57.6 |
| PLA-CNC/PVA−PLA | 5.0 ± 1.1 | 27.1 ± 1.2 | 206.6 ± 45.5 | 1119.9 ± 49.6 |

[a]The error is one standard deviation.



https://doi.org/10.1021/acsapm.4c03954
ACS Appl. Polym. Mater. 2025, 7, 6774−6788

Table 3. Water Vapor Transmission Rate (WVTR) and Water Vapor Permeability (WVP) for PLA, CNC/PVA−PLA, PLA−PLA, and PLA-CNC/PVA−PLA at Different Humidity Conditions and Configurations under the ASTM F1249 Standard (37.8°C)[a]

| sample | humidity [% RH] | configuration* | WVTR [g/(m²·day)] | WVP [g·μm/m²·day·kPa] |
|---|---|---|---|---|
| PLA | 50 | | 131.9 ± 7.7 | 1177.7 ± 35.8 |
| PLA−PLA | 50 | | 68.9 ± 2.7 | 1256.8 ± 48.6 |
| | 90 | | 120.7 ± 0.9 | 1222.4 ± 9.1 |
| CNC/PVA−PLA | 50 | a | 117.8 ± 6.0 | 1181.6 ± 59.9 |
| | | b | 21.3 ± 0.9 | 220.0 ± 8.9 |
| | 90 | a | 242.9 ± 1.1 | 1353.9 ± 6.3 |
| | | b | 93.7 ± 0.6 | 538.4 ± 3.6 |
| PLA-CNC/PVA−PLA | 50 | a | 22.6 ± 3.8 | 452.5 ± 75.6 |
| | | b | 23.4 ± 0.5 | 450.3 ± 10.0 |
| | 90 | a | 90.6 ± 0.8 | 1008.9 ± 9.4 |
| | | b | 98.7 ± 0.6 | 1057.0 ± 6.6 |

[a]The error is one standard deviation. For the configuration, "a" means the side where CNC/PVA from the original PLA substrate faces the high humidity, and "b" means the side where CNC/PVA from the original PLA substrate faces the low humidity.

Table 4. Oxygen and Carbon Dioxide Permeability for PLA, CNC/PVA−PLA, PLA−PLA, and PLA-CNC/PVA−PLA films and the CNC/PVA Coating at 0% RH[a]

| sample | OP × $10^{-16}$ [cm³[STP]·cm/(cm²·s·Pa)] | $CO_2P$ × $10^{-16}$ [cm³[STP]·cm/(cm²·s·Pa)] |
|---|---|---|
| PLA | 240.0 | 1024.3 |
| CNC/PVA−PLA | 3.0 | 15.3 |
| PLA−PLA | 231.3 | 1006.7 |
| PLA-CNC/PVA−PLA | 3.3 | 21.5 |
| CNC/PVA coating | 0.43−0.49 | 1.72−2.56 |

[a]The values for the CNC/PVA coating were calculated by using eq 7. To convert to the relevant SI unit [m³[STP]·m/(m²·s·Pa)], use xP × $10^{-20}$.

increased the WVP values. High water vapor partial pressure caused moisture to penetrate the PLA layer and "plasticized" the CNC/PVA layer, leading to high transport. Regardless, the overall package was about the same as pure PLA, due to the laminated structure. In real-world applications, food packaging does not always need to endure 100 RH% humidity environments and many types of foods like dried fruits and chips that are sensitive to moisture, while their storage conditions more closely resemble dry-cup testing.

To confirm these results using commercially applicable testing, water barrier properties using a Permatran-W 3/34 G WVTR analyzer following ASTM F1249 were performed and are shown in Table 3. Configuration means which side faces the high humidity side. For CNC/PVA−PLA, the front side is the CNC/PVA coating layer and the back side means the bottom PLA layer. For the PLA-CNC/PVA−PLA layer, the front side is the upper PLA layer (the one without a CNC/PVA layer before lamination), and the back side is the lower PLA layer (the one coated with a CNC/PVA layer before lamination).

From Table 3, it is observed that the WVP values of PLA and PLA−PLA were consistent at different humidities, which agrees with the expectations as these two are the same materials with different thicknesses. It should be noted that PLA−PLA has a slightly higher, but statistically significant, WVP than single-layer PLA. We attribute this to the effect of hot roll lamination on the films, which may induce structural relaxation, annealing, or trapping dust to act as defects. The principle reason for performing experiments on laminated bilayers is to see this effect. However, it is small enough to be ignored, here. However, it was found that both humidity and configuration could affect the moisture barrier properties of the samples containing CNC/PVA layers. For the PLA-CNC/PVA−PLA trilayer samples, the WVP value was lower than those of the PLA and PLA−PLA samples, indicating that this trilayer structure could help protect the inner CNC/PVA layer, and the inner layer reduced the WVP, and WVP values of the front and back configurations were almost the same. For the CNC/PVA−PLA samples, the front configuration WVP values were in the same range as those of the PLA and PLA−PLA samples, while the back configuration showed the lowest WVP values. This discrepancy could be due to the following reasons. After the water vapor diffuses through the first PLA layer, for back configuration CNC/PVA−PLA, the CNC/PVA layer faces the 0% RH condition, and the dry state helped protected the integrity of the CNC/PVA layer However, for PLA-CNC/PVA−PLA, after the diffusion through the first PLA layer, the water moisture got "trapped" between the two layers of PLA. Therefore, the actual humidity condition of the CNC/PVA inner layer in the trilayer profile was not the same as the bilayer counterpart. Figure S12 shows a schematic plot and humidity profile of different testing conditions. Regardless, all data confirmed the general result as before: at relatively low humidity, CNC/PVA can improve the water barrier property.

Permeability tests for oxygen and carbon dioxide on PLA, CNC/PVA−PLA, PLA−PLA, and PLA-CNC/PVA−PLA samples were conducted, as food preservation is typically highly dependent on these two gases, due to oxidation in the case of oxygen and respiration of fresh foods in the case of carbon dioxide. Table 4 presents the oxygen permeability (OP) and carbon dioxide permeability ($CO_2P$) rates for these four different materials at 0% RH. For results at 0% RH, it is observed that both oxygen and carbon dioxide permeability rates are significantly reduced in samples with CNC/PVA coatings compared with those without coatings, indicating a substantial improvement in barrier properties. This finding


https://doi.org/10.1021/acsapm.4c03954
ACS Appl. Polym. Mater. 2025, 7, 6774−6788

Table 5. Oxygen Permeability (OP) and Oxygen Transmission Rate (OTR) for PLA, CNC/PVA−PLA, PLA−PLA, and PLA-CNC/PVA−PLA Film Samples at 21.1 °C and 50, 70, and 90% RH[a]

| sample | relative humidity | OP × $10^{-16}$ [$cm^3$[STP]·cm/($cm^2$·s·Pa)] | OTR [$cm^3$[STP]/$m^2$·day] |
|---|---|---|---|
| PLA | 50 | 178.1 ± 3.1 | 563.5 ± 49.5 |
| | 70 | 175.9 ± 3.7 | 558.8 ± 50.5 |
| | 90 | 172.7 ± 4.0 | 549.3 ± 47.2 |
| CNC/PVA−PLA | 50 | 4.7 ± 0.2 | 11.4 ± 0.1 |
| | 70 | 17.4 ± 3.9 | 44.8 ± 10.5 |
| | 90 | 147.2 ± 3.4 | 376.9 ± 7.0 |
| PLA−PLA | 50 | 197.0 ± 5.4 | 267.5 ± 7.4 |
| | 70 | 199.9 ± 0.7 | 272.2 ± 1.2 |
| | 90 | 198.1 ± 0.9 | 268.7 ± 0.5 |
| PLA-CNC/PVA−PLA | 50 | 7.8 ± 2.0 | 10.3 ± 2.5 |
| | 70 | 25.0 ± 5.7 | 32.8 ± 7.3 |
| | 90 | 150.6 ± 26.3 | 198.1 ± 35.0 |

[a]To convert to the relevant SI unit [$m^3$[STP]·m/($m^2$·s·Pa)], use OP × $10^{-20}$. The error is one standard deviation.

aligns with results reported in the previous literature,[4] with a decrease in oxygen permeability and an increase in carbon dioxide permeability. Additionally, the concentration of $CO_2$P was considerably higher than that of OP. Permeability depends on the interaction between the gaseous penetrant and the plastic substrate. While typically considered "non-polar", $CO_2$ is a linear molecule with the central carbon atom carrying a partial positive charge and the two terminal oxygen atoms carrying a partial negative charge. While this means that formally the two dipoles cancel, the charge distribution results in a quadrupole moment in the $CO_2$ molecule. Polar polymer molecules contain permanent dipole moments, and these polar groups can experience strong electrostatic and induction forces, with the quadrupole moment of the $CO_2$ molecule. These interactions between $CO_2$ and polar polymers facilitate the penetration of $CO_2$ molecules into the polymer matrix, thereby increasing the solubility and diffusivity of $CO_2$ in these types of polymers, which explains why $CO_2$ permeability is generally higher than $O_2$ in polar plastic films. Overall, the result of oxygen and carbon dioxide permeability values for the CNC/PVA coating layer of this research is very close to values reported by other papers.[4,14]

$O_2$ permeability values were also measured at 21.1 °C, 50, 70, and 90% RH using an Ox-Tran 22/2 L OTR analyzer (Ametek Mocon, Minneapolis, MN) at a 1 atm partial pressure difference of oxygen between two sides. Table 5 shows the $O_2$ permeability for the four different films. Comparing the values from Tables 4 and 5, it could be found that at both conditions, the CNC/PVA layer helped reduce the $O_2$ permeability by about 2 orders of magnitude. The permeability of every sample decreased due to lower pressure differences. For the results in Table 4, the permeability results were collected under 50 psi (~3.4 atm) upstream pressure, while the permeability results listed in Table 5 were collected under 1 atm. Interestingly, the CNC/PVA−PLA samples showed a slightly lower OP against PLA-CNC/PVA−PLA under all conditions. By using eq 4, the CNC/PVA layer from CNC/PVA−PLA showed a permeability of around 6.44 × $10^{-15}$ $cm^3$[STP]·cm/($cm^2$·s·Pa) at 21.1 °C, 90% RH, while the CNC/PVA layer from PLA-CNC/PVA−PLA PLA showed a permeability of around 3.69 × $10^{-15}$ $cm^3$[STP]·cm/($cm^2$·s·Pa) at 21.1 °C, 90% RH. Therefore, the outer PLA layer still showed some degree of protection for the inner CNC/PVA layer at high humidity conditions.

Another experiment was designed to characterize the resistance of the CNC layers in the multilayers after a high-low humidity cycle. It was found that the oxygen permeability of CNC/PVA−PLA films was 3.13 × $10^{-15}$ $cm^3$[STP]·cm/($cm^2$·s·Pa), and the oxygen permeability of PLA-CNC/PVA−PLA films was 4.79 × $10^{-16}$ $cm^3$[STP]·cm/($cm^2$·s·Pa). For CNC/PVA−PLA samples, the $O_2$ permeability value was about 1000% of the same sample without the high-low humidity cycle, indicating that the CNC/PVA layer was eventually damaged. However, for the PLA-CNC/PVA−PLA sample, the $O_2$ permeability was almost the same as before, meaning that the outer PLA layer protected the inner CNC/PVA layer from being washed away, and its barrier performance could be restored after a high-low humidity cycle. Furthermore, the oxygen permeability of PLA-CNC/PVA−PLA undergoing the dry-water-dry condition was 4.29 × $10^{-15}$ $cm^3$[STP]·cm/($cm^2$·s·Pa). At this extremely wet condition, it was not surprising that the permeability of the sample increased about ten times. However, the permeability value of this sample was still around 20% of the value of PLA, indicating that outer PLA can protect the inner CNC/PVA layer, and the multilayer film still serves as a barrier toward oxygen even under relatively extreme conditions.

**3.5. Change of the Fruit Color, Weight, and Oxygen Level during the Fruit Storage Test.** Browning is a common phenomenon observed in many fruits and vegetables when they are cut, bruised, or damaged. This process is responsible for the brown coloration that appears on the surface of produce such as apples, pears, avocados, peaches, eggplants, etc. The primary cause of browning is the oxidation of phenolic compounds by enzymes, particularly polyphenol oxidase (PPO). When plant cells are damaged, PPO encounters phenolic compounds and oxygen, catalyzing a reaction that produces melanin-like pigments. While enzymatic browning does not typically affect the safety or nutritional value of food, it can significantly impact its appearance, taste, and texture, often leading to reduced consumer acceptability, shortening the shelf life of fresh produce, and economic losses in the food industry. This process is particularly problematic in fresh-cut fruits and vegetables, juices, and minimally processed foods. Common approaches to inhibit enzymatic browning include using thermal treatments to inactivate enzymes,[51] oxygen exclusion through packaging or edible coatings,[52,53] genetic modification to produce varieties with reduced PPO activity,[54] and the addition of acids like ascorbic acid (vitamin C) or citric acid.[55] Among these methods, using oxygen barrier materials as packaging materials or edible coatings is a


https://doi.org/10.1021/acsapm.4c03954
ACS Appl. Polym. Mater. 2025, 7, 6774−6788

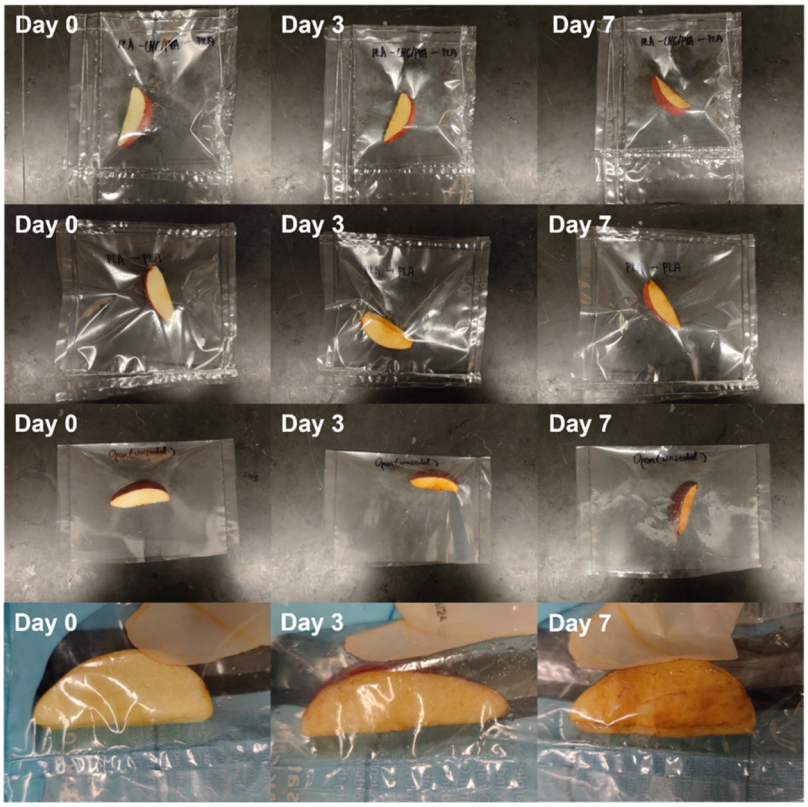


**Figure 7.** Fresh-cut apple sliced in different packages at room-temperature conditions (~23 °C, ~50% RH). From top to bottom: PLA-CNC/PVA−PLA, PLA−PLA, unsealed, and commercial bags.

promising approach due to its low cost and ease of mass production. Wongthanaroj et al.[52] explored using PLA/CNC nanocomposite films to protect fresh-cut avocados. PLA and dry CNCs were mixed and compounded, then extruded by a twin-screw extruder, and rolled into films with a thickness of 60 $\mu$m. Later, avocados were cut into halves and packed in bags made of PLA and PLA/CNC composite films, with analysis by quantification of color change on the surface. It was found that for both room-temperature and chilled-temperature conditions, the PLA/CNC nanocomposite film could preserve the avocado halves longer, with an extension of 1.3 days at room temperature and 5.4 days at chilled temperatures regarding the browning due to the higher oxygen barrier properties of the PLA/CNC film over the pure PLA film.

In this research, visual appearance, color change, and changes in mass were recorded to characterize the freshness of the freshly cut "red delicious" apple slices. The change in the oxygen level inside was recorded in bags without apple slices to avoid the mutual interference between the respiration effect of apple slices and the diffusion of oxygen from outside to inside as well as to test the oxygen barrier capability of the materials when they are made into packaging bags for actual use. Figure S13 shows the color parameters under different testing conditions. In the Lab scale, $L^*$ (lightness) is defined as $L = 0$ (black) and $L = 100$ (white). The $a^*$ axis represents the spectrum between green and red, with negative values toward green and positive values toward red hues; and the $b^*$ axis represents the spectrum between blue and yellow, with negative values toward and positive values toward yellow. It was found that the $a^*$ and $b^*$ values of all samples exhibited an increasing trend as the time went by. However, the L* values fluctuated between 60 and 70 without an obvious trend and did not decrease until $b^*$ values plateaued at around 20. The increase in $a^*$ and $b^*$ values was attributed to browning of the apple slice surface. Among these changes, the increase in $b^*$ values was found to be most pronounced. Consequently, the change in $b^*$ values was utilized as a criterion to determine whether the apple slices had undergone browning. A deceleration in the growth trend was observed when the $b^*$ value approached approximately 20. It was found that the shelf life was extended by approximately 5 days when PLA-CNC/PVA−PLA was employed as the packaging material, as compared to samples packaged with PLA−PLA or commercial packaging bags. Moreover, it was observed that for the samples packaged with the PLA-CNC/PVA−PLA material, no significant differences in Lab color values were detected between samples stored at room temperature and those refrigerated. This observation suggested that the primary factor contributing to apple browning was not temperature, but oxygen concentration. The effectiveness of PLA-CNC/PVA−PLA in providing oxygen barrier properties was demonstrated to be substantial under both room temperature and refrigerated conditions. Photos of apple slices under different conditions are shown in Figures 7, S13 and S14. It must be noted that, commercially, apple packaging is coated with ascorbic acid to prevent browning and these were not. Thus, it is not an "apples-to-apples" comparison with commercial packaging. However, here the PLA-CNC/PVA−PLA trilayer films performed as well or better in preventing the oxidation of fruit as compared to commercial PET bags.

The weight loss rates of various samples are listed in Figure 8. It was observed that the commercial bag group exhibited the lowest water loss rate, which was attributed to its PET composition, as shown in Figure S16. Biaxially oriented PET


https://doi.org/10.1021/acsapm.4c03954
ACS Appl. Polym. Mater. 2025, 7, 6774−6788

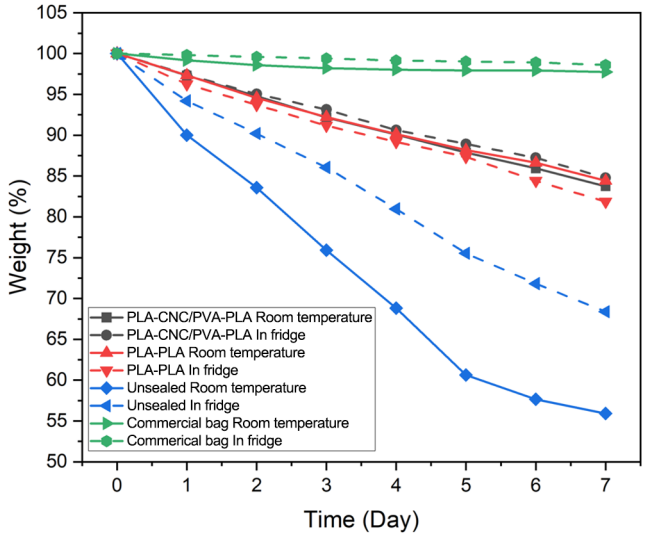


**Figure 8.** Weight loss of different bags under different testing conditions.

has significantly lower water permeability than PLA. The water loss rates of the PLA−PLA group and the PLA-CNC/PVA−PLA group were found to be essentially equivalent, which was consistent with the WVTR test results reported earlier in this study. Furthermore, no significant correlation was detected between the water loss rates at room temperature and refrigerated conditions in different groups. It was noted that the water loss rate could be influenced by multiple factors, including the mass and size of apple slices, fruit flesh surface area, temperature and humidity differences, and sealing quality of the packaging.

Figure 9 depicts the oxygen concentration measurements within bags made from PLA−PLA and PLA-CNC/PVA−PLA films. The initial oxygen concentration was 0.4% (v/v). An oxygen concentration sensor was placed within each bag, and the data were recorded daily. The variation in the oxygen

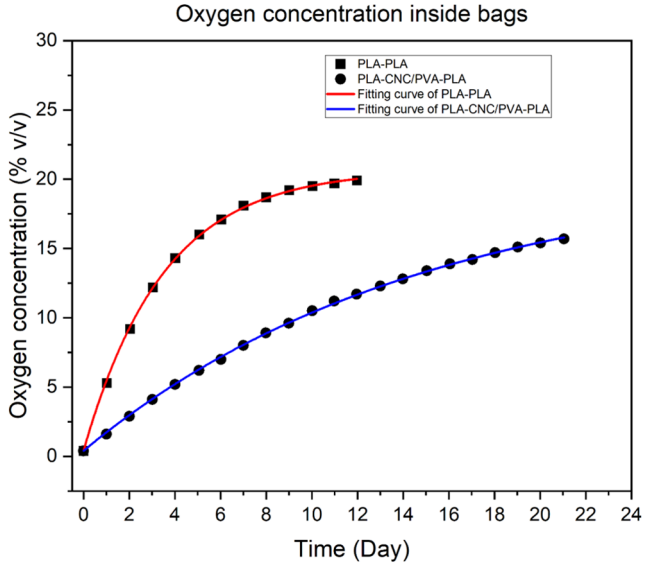


**Figure 9.** Change of the oxygen concentration in PLA-CNC/PVA−PLA and PLA−PLA bags.

concentration within the packaging bags was found to adhere to the following model:

$$c(t) = c_0 + A(1 - e^{-t/\tau}) \quad (8)$$

where $c(t)$ is the oxygen concentration at time $t$, $c_0$ is the initial oxygen concentration at $t = 0$, $A$ is the parameter that represents the difference between the initial oxygen concentration and the theoretical final oxygen concentration, and $\tau$ is a time constant that characterizes how long it takes for the system to reach the limit. In our case, the initial oxygen concentration $c_0 = 0.4\%$.

The equation for the oxygen concentration inside the PLA−PLA bag is

$$c(t) = 0.4 + 20.29(1 - e^{-t/3.50})$$

The equation for the oxygen concentration inside the PLA-CNC/PVA−PLA bag is

$$c(t) = 0.4 + 20.31(1 - e^{-t/14.82})$$

The R-square values of both fitting curves were more than 0.999.

These equations indicate that the time required to reach the same oxygen concentration internally was approximately four times more for the PLA-CNC/PVA−PLA packaging compared to the PLA−PLA packaging. This observation suggested that superior oxygen barrier properties were exhibited by the PLA-CNC/PVA−PLA packaging, which was consistent with the previously conducted fresh-cut apple slice storage test. However, it should be noted that the OTR and OP tests demonstrated the oxygen barrier performance of PLA-CNC/PVA−PLA to be approximately one hundred times that of PLA−PLA. Regarding this discrepancy, it is postulated that the difference can be attributed to the sealing process, wherein PLA-to-PLA contact is established along each edge. The CNC/PVA layer, being situated internally, is unable to provide protection at the edges, resulting in higher oxygen transmission rates at the edges compared to those on the surface. Nevertheless, it could be concluded that superior oxygen barrier properties were still demonstrated by the PLA-CNC/PVA−PLA packaging.

In addition, the same method was employed to test the oxygen concentration within commercial bags. The results indicated that the oxygen concentration increased from 0.2 to 19.5% in less than 24 h, demonstrating the poor oxygen barrier performance of the packaging. Most commercially available fresh-cut fruit packages maintain freshness by incorporating vitamin C as an acid source and an antioxidant. In this study, the biodegradable and sustainable PLA-CNC/PVA−PLA material provides a new approach to food packaging.

## 4. CONCLUSIONS

In summary, a sustainable and biodegradable trilayer packaging film with high oxygen and carbon dioxide barrier properties was successfully fabricated by blade-coating a shear-oriented CNC/PVA mixture onto a PLA substrate followed by hot roll lamination with another PLA film. The blade-coating method produced a thin (~6 $\mu$m), highly aligned (S = 0.84) CNC/PVA layer that significantly reduced gas permeability while maintaining optical transparency, unlike other works on trilayer CNC films. The laminated PLA outer layers helped to shield the moisture-sensitive CNC/PVA layer. While the improvement in the water vapor barrier was limited due to the


https://doi.org/10.1021/acsapm.4c03954
ACS Appl. Polym. Mater. 2025, 7, 6774−6788

inherent hydrophilicity of CNC/PVA, the trilayer films still showed lower water vapor transmission rates compared to neat PLA under moderate humidity conditions. Importantly, first-of-its-kind application specific fruit storage testing of these types of materials showed that PLA-CNC/PVA−PLA-based packaging could extend the shelf life of fresh-cut apple slices in terms of browning. When compared to commercial bags, bags of these films outperformed PET on oxidation/browning of fruits but were appreciably worse in water loss. Thus, these biobased multilayer flexible film bags are likely better suited for low-water, oily fruits without an acid coating, rather than apples, but have great potential for sustainable food storage.

## ■ ASSOCIATED CONTENT

### Data Availability Statement

The data that support the findings of this study are available on request from the corresponding author, J.P.Y., upon reasonable request.

### Supporting Information

The Supporting Information is available free of charge at https://pubs.acs.org/doi/10.1021/acsapm.4c03954.

Locations of the $L^*a^*b^*$ test on apple slices; FTIR curves of CNC/PVA, PLA, and CNC/PVA−PLA; stress vs strain curves of four films; photos of four types of films after the tensile test; schematic plot of PLA−PLA and CNC/PVA−PLA; photos for peeling tests and tape tests; transparency of films; transmittance values for the coated sample between linear cross-polarizers; schematic plot of water vapor permeation for multilayer films; $L^*a^*b^*$ values vs time; photos of fruit tests; and FTIR curve of the commercial PET bag (PDF)

## ■ AUTHOR INFORMATION


### Corresponding Author

**Jeffrey P. Youngblood** − *School of Materials Engineering, Purdue University, West Lafayette, Indiana 47907, United States;* orcid.org/0000-0002-8720-8642; Email: jpyoungb@purdue.edu

### Authors

**Jingxuan Zhang** − *School of Materials Engineering, Purdue University, West Lafayette, Indiana 47907, United States;* orcid.org/0000-0002-4189-136X

**Yirou Wang** − *School of Materials Engineering, Purdue University, West Lafayette, Indiana 47907, United States;* orcid.org/0000-0002-7128-7657

**Darien Anders Dewar** − *School of Materials Engineering, Purdue University, West Lafayette, Indiana 47907, United States*

**Akshat Verma** − *School of Materials Engineering, Purdue University, West Lafayette, Indiana 47907, United States*

**Nazmul Haque** − *School of Materials Engineering, Purdue University, West Lafayette, Indiana 47907, United States*

**Ronaldo Franjul** − *School of Materials Engineering, Purdue University, West Lafayette, Indiana 47907, United States*

**Nicole Stark** − *Forest Products Laboratory, United States Department of Agriculture, Madison, Wisconsin 53726, United States;* orcid.org/0000-0002-9246-5205

**Chelsea S. Davis** − *School of Materials Engineering, Purdue University, West Lafayette, Indiana 47907, United States; Department of Mechanical Engineering, University of Delaware, Newark, Delaware 19716, United States;* orcid.org/0000-0002-0383-7717

Complete contact information is available at: https://pubs.acs.org/10.1021/acsapm.4c03954


### Author Contributions

#J.Z. and Y.W. contributed equally. J.Z. and J.P.Y. designed the experiment. J.Z. prepared the materials and performed the coating and lamination. J.Z. and Y.W. prepared SEM samples and analyzed SEM images. Y.W. prepared CNC/PVA−PLA samples and analyzed them under the cross-polarizer microscope. A.V. contributed to the uniaxial tensile test. J.Z. prepared adhesion test samples. J.Z., N.H., and C.D. contributed to adhesion tests and analyses. J.Z. prepared AFM samples and conducted AFM characterization. J.Z., Y.W., and A.V. contributed to UV−vis tests and analyses. J.Z. conducted the WVTR tests. J.Z., Y.W., and N.S. contributed to the gas barrier performance tests. J.Z. and D.D. prepared fruit storage test samples and conducted the fruit tests. J.Z. wrote the manuscript. Y.W., D.D, A.V., R.F., and J.P.Y revised it. All authors have given approval to the final version of the manuscript.


### Funding

This research was primarily funded in part by the Purdue Research Foundation under Grant Numbers 60000034 and 17001072 and the US Endowment for Forestry and Communities-Public-Private Partnership for Nanotechnology (P3Nano) under Grant No. 22-00466. This research was also partially sponsored by SERDP/ESTCP under Grant No. WP22-3269 and ARPA-E under Grant No. 14000739.


### Notes

The authors declare no competing financial interest.

## ■ REFERENCES


(1) Ncube, L. K.; Ude, A. U.; Ogunmuyiwa, E. N.; Zulkifli, R.; Beas, I. N. An Overview of Plasticwaste Generation and Management in Food Packaging Industries. *Recycling* **2021**, *6* (1), 1−25.

(2) Someya, T.; Bao, Z.; Malliaras, G. G. The Rise of Plastic Bioelectronics. *Nature* **2016**, *540* (7633), 379−385.

(3) Záleská, M.; Pavlíková, M.; Pokorný, J.; Jankovský, O.; Pavlík, Z.; Černý, R. Structural, Mechanical and Hygrothermal Properties of Lightweight Concrete Based on the Application of Waste Plastics. *Constr. Build. Mater.* **2018**, *180*, 1−11.

(4) Nuruddin, M.; Chowdhury, R. A.; Szeto, R.; Howarter, J. A.; Erk, K. A.; Szczepanski, C. R.; Youngblood, J. P. Structure-Property Relationship of Cellulose Nanocrystal-Polyvinyl Alcohol Thin Films for High Barrier Coating Applications. *ACS Appl. Mater. Interfaces* **2021**, *13* (10), 12472−12482.

(5) Rochman, C. M.; Browne, M. A. Classify Plastic Waste as Hazardous (Types of Externalities Caused by Consumption of Plastic Bags). *Nature* **2013**, *494* (3), 169−171.

(6) Morales-Caselles, C.; Viejo, J.; Martí, E.; González-Fernández, D.; Pragnell-Raasch, H.; González-Gordillo, J. I.; Montero, E.; Arroyo, G. M.; Hanke, G.; Salvo, V. S.; Basurko, O. C.; Mallos, N.; Lebreton, L.; Echevarría, F.; van Emmerik, T.; Duarte, C. M.; Gálvez, J. A.; van Sebille, E.; Galgani, F.; García, C. M.; Ross, P. S.; Bartual, A.; Ioakeimidis, C.; Markalain, G.; Isobe, A.; Cózar, A. An Inshore−Offshore Sorting System Revealed from Global Classification of Ocean Litter. *Nat. Sustain.* **2021**, *4* (6), 484−493.

(7) Pinheiro, H. T.; MacDonald, C.; Santos, R. G.; Ali, R.; Bobat, A.; Cresswell, B. J.; Francini-Filho, R.; Freitas, R.; Galbraith, G. F.; Musembi, P.; Phelps, T. A.; Quimbayo, J. P.; Quiros, T. E. A. L.; Shepherd, B.; Stefanoudis, P. V.; Talma, S.; Teixeira, J. B.; Woodall, L. C.; Rocha, L. A. Plastic Pollution on the World's Coral Reefs. *Nature* **2023**, *619* (7969), 311−316.

(8) Browne, M. A.; Dissanayake, A.; Galloway, T. S.; Lowe, D. M.; Thompson, R. C. Ingested Microscopic Plastic Translocates to the Circulatory System of the Mussel, Mytilus Edulis (L.). *Environ. Sci. Technol.* **2008**, *42* (13), 5026−5031.
(9) Lithner, D.; Larsson, A.; Dave, G. Environmental and Health Hazard Ranking and Assessment of Plastic Polymers Based on Chemical Composition. *Sci. Total Environ.* **2011**, *409* (18), 3309−3324.
(10) Teuten, E. L.; Saquing, J. M.; Knappe, D. R. U.; Barlaz, M. A.; Jonsson, S.; Björn, A.; Rowland, S. J.; Thompson, R. C.; Galloway, T. S.; Yamashita, R.; Ochi, D.; Watanuki, Y.; Moore, C.; Viet, P. H.; Tana, T. S.; Prudente, M.; Boonyatumanond, R.; Zakaria, M. P.; Akkhavong, K.; Ogata, Y.; Hirai, H.; Iwasa, S.; Mizukawa, K.; Hagino, Y.; Imamura, A.; Saha, M.; Takada, H. Transport and Release of Chemicals from Plastics to the Environment and to Wildlife. *Philos. Trans. R. Soc., B* **2009**, *364* (1526), 2027−2045.
(11) vom Saal, F. S.; Hughes, C. An Extensive New Literature Concerning Low-Dose Effects of Bisphenol A Shows the Need for a New Risk Assessment. *Environ. Health Perspect.* **2005**, *113* (8), 926−933.
(12) Moon, R. J.; Martini, A.; Nairn, J.; Simonsen, J.; Youngblood, J. Cellulose Nanomaterials Review: Structure, Properties and Nanocomposites. *Chem. Soc. Rev.* **2011**, *40* (7), 3941−3994.
(13) Foster, E. J.; Moon, R. J.; Agarwal, U. P.; Bortner, M. J.; Bras, J.; Camarero-Espinosa, S.; Chan, K. J.; Clift, M. J. D.; Cranston, E. D.; Eichhorn, S. J.; Fox, D. M.; Hamad, W. Y.; Heux, L.; Jean, B.; Korey, M.; Nieh, W.; Ong, K. J.; Reid, M. S.; Renneckar, S.; Roberts, R.; Shatkin, J. A.; Simonsen, J.; Stinson-Bagby, K.; Wanasekara, N.; Youngblood, J. Current Characterization Methods for Cellulose Nanomaterials. *Chem. Soc. Rev.* **2018**, *47* (8), 2609−2679.
(14) Chowdhury, R. A.; Nuruddin, M.; Clarkson, C.; Montes, F.; Howarter, J.; Youngblood, J. P. Cellulose Nanocrystal (CNC) Coatings with Controlled Anisotropy as High-Performance Gas Barrier Films. *ACS Appl. Mater. Interfaces* **2019**, *11* (1), 1376−1383.
(15) Lagaron, J. M.; Catala, R.; Gavara, R. Structural Characteristics de Ning High Barrier Properties in Polymeric Materials. *Mater. Sci. Technol.* **2004**, *20* (1), 1−7.
(16) Zhang, J.; Youngblood, J. P. Cellulose Nanofibril (CNF)-Coated PFAS-Free, Grease-Resistant All-Bio-Based Molded Pulp Containers for Food Packaging. *ACS Appl. Polym. Mater.* **2023**, *5* (7), 5696−5706.
(17) Wang, J.; Gardner, D. J.; Stark, N. M.; Bousfield, D. W.; Tajvidi, M.; Cai, Z. Moisture and Oxygen Barrier Properties of Cellulose Nanomaterial-Based Films. *ACS Sustainable Chem. Eng.* **2018**, *6* (1), 49−70.
(18) Hubbe, M. A.; Ferrer, A.; Tyagi, P.; Yin, Y.; Salas, C.; Pal, L.; Rojas, O. J. Nanocellulose in Thin Films, Coatings, and Plies for Packaging Applications: A Review. *BioResources* **2016**, *12* (1), 2143−2233.
(19) Prathapan, R.; Tabor, R. F.; Garnier, G.; Hu, J. Recent Progress in Cellulose Nanocrystal Alignment and Its Applications. *ACS Appl. Bio Mater.* **2020**, *3* (4), 1828−1844.
(20) Habibi, Y.; Lucia, L. A.; Rojas, O. J. Cellulose Nanocrystals: Chemistry, Self-Assembly, and Applications. *Chem. Rev.* **2010**, *110* (6), 3479−3500.
(21) Revol, J. F.; Bradford, H.; Giasson, J.; Marchessault, R. H.; Gray, D. G. Helicoidal Self-Ordering of Cellulose Microfibrils in Aqueous Suspension. *Int. J. Biol. Macromol.* **1992**, *14* (3), 170−172.
(22) Orts, W. J.; Godbout, L.; Marchessault, R. H.; Revol, J. F. Enhanced Ordering of Liquid Crystalline Suspensions of Cellulose Microfibrils: A Small Angle Neutron Scattering Study. *Macromolecules* **1998**, *31* (17), 5717−5725.
(23) Ebeling, T.; Paillet, M.; Borsali, R.; Diat, O.; Dufresne, A.; Cavaillé, J. Y.; Chanzy, H. Shear-Induced Orientation Phenomena in Suspensions of Cellulose Microcrystals, Revealed by Small Angle X-Ray Scattering. *Langmuir* **1999**, *15* (19), 6123−6126.
(24) Chowdhury, R. A.; Peng, S. X.; Youngblood, J. Improved Order Parameter (Alignment) Determination in Cellulose Nanocrystal (CNC) Films by a Simple Optical Birefringence Method. *Cellulose* **2017**, *24* (5), 1957−1970.
(25) Haywood, A. D.; Davis, V. A. Effects of Liquid Crystalline and Shear Alignment on the Optical Properties of Cellulose Nanocrystal Films. *Cellulose* **2017**, *24* (2), 705−716.
(26) Hoeger, I.; Rojas, O. J.; Efimenko, K.; Velev, O. D.; Kelley, S. S. Ultrathin Film Coatings of Aligned Cellulose Nanocrystals from a Convective-Shear Assembly System and Their Surface Mechanical Properties. *Soft Matter* **2011**, *7* (5), 1957−1967.
(27) Pullawan, T.; Wilkinson, A. N.; Eichhorn, S. J. Influence of Magnetic Field Alignment of Cellulose Whiskers on the Mechanics of All-Cellulose Nanocomposites. *Biomacromolecules* **2012**, *13* (8), 2528−2536.
(28) Li, D.; Liu, Z.; Al-Haik, M.; Tehrani, M.; Murray, F.; Tannenbaum, R.; Garmestani, H. Magnetic Alignment of Cellulose Nanowhiskers in an All-Cellulose Composite. *Polym. Bull.* **2010**, *65* (6), 635−642.
(29) Kim, J.; Chen, Y.; Kang, K. S.; Park, Y. B.; Schwartz, M. Magnetic Field Effect for Cellulose Nanofiber Alignment. *J. Appl. Phys.* **2008**, *104* (9), No. 096104, DOI: 10.1063/1.3006140.
(30) Kvien, I.; Oksman, K. Orientation of Cellulose Nanowhiskers in Polyvinyl Alcohol. *Appl. Phys. A* **2007**, *87* (4), 641−643.
(31) Park, J.; Lu, W. Orientation of Core-Shell Nanoparticles in an Electric Field. *Appl. Phys. Lett.* **2007**, *91* (5), 6365−6367.
(32) Erukhimovich, I.; de la Cruz, M. O. Phase Equilibria and Charge Fractionation in Polydisperse Polyelectrolyte Solutions. *J. Polym. Sci., Part B: Polym. Phys.* **2004**, 1430−1436.
(33) Frka-Petesic, B.; Jean, B.; Heux, L. Electrohydrodynamic Convection Instabilities Observed in Suspensions of Cellulose Nanocrystals. *Cellulose* **2023**, *30* (13), 8311−8323.
(34) Chowdhury, R. A.; Clarkson, C.; Youngblood, J. Continuous Roll-to-Roll Fabrication of Transparent Cellulose Nanocrystal (CNC) Coatings with Controlled Anisotropy. *Cellulose* **2018**, *25* (3), 1769−1781.
(35) Nuruddin, M.; Chowdhury, R. A.; Lopez-Perez, N.; Montes, F. J.; Youngblood, J. P.; Howarter, J. A. Influence of Free Volume Determined by Positron Annihilation Lifetime Spectroscopy (PALS) on Gas Permeability of Cellulose Nanocrystal Films. *ACS Appl. Mater. Interfaces* **2020**, *12* (21), 24380−24389.
(36) Nuruddin, M.; Korani, D. M.; Jo, H.; Chowdhury, R. A.; Montes, F. J.; Howarter, J. A.; Youngblood, J. P. Gas and Water Vapor Barrier Performance of Cellulose Nanocrystal-Citric Acid-Coated Polypropylene for Flexible Packaging. *ACS Appl. Polym. Mater.* **2020**, *2* (11), 4405−4414.
(37) Shrestha, S.; Diaz, J. A.; Ghanbari, S.; Youngblood, J. P. Hygroscopic Swelling Determination of Cellulose Nanocrystal (CNC) Films by Polarized Light Microscopy Digital Image Correlation. *Biomacromolecules* **2017**, *18* (5), 1482−1490.
(38) Koppolu, R.; Lahti, J.; Abitbol, T.; Swerin, A.; Kuusipalo, J.; Toivakka, M. Continuous Processing of Nanocellulose and Polylactic Acid into Multilayer Barrier Coatings. *ACS Appl. Mater. Interfaces* **2019**, *11* (12), 11920−11927.
(39) Le Gars, M.; Dhuiège, B.; Delvart, A.; Belgacem, M. N.; Missoum, K.; Bras, J. High-Barrier and Antioxidant Poly(Lactic Acid)/Nanocellulose Multilayered Materials for Packaging. *ACS Omega* **2020**, *5* (36), 22816−22826.
(40) Chen, C.; Wang, L.; Shams Es-haghi, S.; Tajvidi, M.; Wang, J.; Gardner, D. J. Biodegradable and Recyclable Bio-Based Laminated Films of Poly (Lactic Acid) and Cellulose Nanocrystals for Food Barrier Packaging. *Food Packag. Shelf Life* **2024**, *42*, No. 101244.
(41) Chowdhury, R. A.; Clarkson, C.; Apalangya, V. A.; Islam, S. M. N.; Youngblood, J. P. Roll-to-Roll Fabrication of Cellulose Nanocrystal-Poly(Vinyl Alcohol) Composite Coatings with Controlled Anisotropy. *Cellulose* **2018**, *25* (11), 6547−6560.
(42) ASTM D1746. *ASTM D1746 Standard Test Method for Transparency of Plastic Sheeting*; ASTM, 2015.
(43) ASTM E96/E96M-22a. *Standard Test Methods for Gravimetric Determination of Water Vapor Transmission*; ASTM, 2022.

(44) Horst, C.; Tetsuya, S.; Smith, L. *Springer Handbook of Materials Measurement Methods*; Springer: Berlin, Heidelberg, 2006.
(45) Zeman, S.; Kubík, L. Permeability of Polymeric Packaging Materials. *Technol. Sci.* **2007**, *10*, 26−34.
(46) Ashter, S. A. Mechanics of Materials. In *Thermoforming of Single and Multilayer Laminates*; Elsevier, 2014; pp 123−145.
(47) Chowdhury, R. A. *Roll-To-Roll Fabrication of Cellulose Nanocrystal Nanocomposite for Gas Barrier and Thermal Management Applications*; Purdue University, 2019.
(48) Fortunati, E.; Puglia, D.; Luzi, F.; Santulli, C.; Kenny, J. M.; Torre, L. Binary PVA Bio-Nanocomposites Containing Cellulose Nanocrystals Extracted from Different Natural Sources: Part I. *Carbohydr. Polym.* **2013**, *97* (2), 825−836.
(49) Ozer, A. The Effect of Substrate Roughness on Tape Peeling. *Int. J. Adhes. Adhes.* **2015**, *62*, 14−17.
(50) Guzman-Puyol, S.; Benítez, J. J.; Heredia-Guerrero, J. A. Transparency of Polymeric Food Packaging Materials. *Food Res. Int.* **2022**, *161*, No. 111792, DOI: 10.1016/j.foodres.2022.111792.
(51) Umair, M.; Jabeen, S.; Ke, Z.; Jabbar, S.; Javed, F.; Abid, M.; Rehman Khan, K. ur.; Ji, Y.; Korma, S. A.; El-Saadony, M. T.; Zhao, L.; Cacciotti, I.; Mariana Gonçalves Lima, C.; Adam Conte-Junior, C. Thermal Treatment Alternatives for Enzymes Inactivation in Fruit Juices: Recent Breakthroughs and Advancements. *Ultrason. Sonochem.* **2022**, *86*, No. 105999, DOI: 10.1016/j.ultsonch.2022.105999.
(52) Wongthanaroj, D.; Jessmore, L. A.; Lin, Y.; Bergholz, T. M.; Stark, N. M.; Sabo, R. C.; Matuana, L. M. Sustainable and Eco-Friendly Poly (Lactic Acid)/Cellulose Nanocrystal Nanocomposite Films for the Preservation of Oxygen-Sensitive Food. *Appl. Food Res.* **2022**, *2* (2), No. 100222.
(53) Singkhonrat, J.; Ovatlarnporn, C.; Khan, K. ur R.; Basit, A.; Suksuwan, A.; Nalinbenjapun, S.; Sripetthong, S.; Korma, S. A.; Cacciotti, I. Fabrication of Different Nanocrystal (CNC)-Based Coatings for the Enhancement of Shelf Life and Quality of Minimally Processed Fruits. *Cellulose* **2023**, *30* (18), 11521−11536.
(54) González, M. N.; Massa, G. A.; Andersson, M.; Turesson, H.; Olsson, N.; Fält, A. S.; Storani, L.; Décima Oneto, C. A.; Hofvander, P.; Feingold, S. E. Reduced Enzymatic Browning in Potato Tubers by Specific Editing of a Polyphenol Oxidase Gene via Ribonucleoprotein Complexes Delivery of the CRISPR/Cas9 System. *Front. Plant Sci.* **2020**, *10*, No. 497481.
(55) Bhat, T. A.; Rather, A. H.; Hussain, S. Z.; Naseer, B.; Qadri, T.; Nazir, N. Efficacy of Ascorbic Acid, Citric Acid, Ethylenediaminetetra-acetic Acid, and 4-Hexylresorcinol as Inhibitors of Enzymatic Browning in Osmo-Dehydrated Fresh Cut Kiwis. *J. Food Meas. Charact.* **2021**, *15* (5), 4354−4370.




https://doi.org/10.1021/acsapm.4c03954
ACS Appl. Polym. Mater. 2025, 7, 6774−6788